Atmospheric
Chemistry
and Physics

Supplement of

The influence of multiple groups of biological ice nucleating particles on microphysical properties of mixed-phase clouds observed during MC3E

Sachin Patade et al.

Correspondence to: Sachin Patade (sachin.patade@nateko.lu.se)

1. Aircraft Instrumentation during MC3E:

The Citation aircraft was equipped with a standard suite of meteorological instruments, which provided high-resolution measurements of temperature, pressure, and humidity. In addition, it carried microphysical probes for cloud and precipitation, and liquid water content, as listed in Table S1. Particle size distributions (PSDs) from cloud to precipitation particle sizes were measured with various probes, including a 2D Cloud Imaging Probe (2D-C), a Cloud Imaging Probe (CIP), and a High-Volume Precipitation Spectrometer Probe (HVPS). The 2D-C and CIP probe data were processed objectively using the algorithm developed at the National Center for Atmospheric Research (NCAR) to mitigate artifacts produced by shattering on the probes' leading edges (Field et al. 2006). The 2D-C probe was equipped with anti-shattering tips (Korolev et al., 2011), while the CIP did not have anti-shattering tips. The size distribution of cloud drops with diameters from 2 to 50 μm was measured using a Cloud Droplet Probe (CDP). A King hot-wire liquid water content (LWC) probe measured the LWC. Vertical velocity is derived from air motion sensing systems available on the research aircraft.

2. Vertical sounding characteristics

The skew-T plot from the radiosonde sounding conducted on 20 May 2011, at (00 UTC) is shown in Figure S1a. The skew-T plot shows the vertical sounding before the formation of deep convection. It shows that the surface-based Convective Available Potential Energy (CAPE) for this case was 2400 J kg^{-1}, and the Lifting Condensation Level (LCL) was located at 840 hPa. The temperature at LCL, which is generally at the same height as the convective cloud base, was 15°C. The water vapor mixing ratio at the surface was around 11.8 gkg^{-1} which decrease rapidly to 2 gkg^{-1} at 5 km (Figure S1b).

3. Description of Empirical formulation for PBAP INPs

The empirical formulation by PT21 is for multiple groups of PBAPs that include: - 1) fungal spores (FNG), 2) bacteria (BCT), 3) pollen (PLN), 4) viral particles, plant/animal detritus (DTS), 5) algae (ALG).

For X= FNG, PLN, BCT, and DTS

$$n_{IN\_BIO,X} = \int_{\log[0.1\ \mu m]}^{\infty} \{1 - \exp[-\mu_X]\} \times \frac{dn_X}{d\log D_X} d\log D_X, \qquad (1)$$

$$\mu_X = H_X(S_i, T)\ \xi(T)\ \times \text{MIN}\{[\exp(-\gamma_X T) - 1], 40\} \times \frac{1}{\omega_{X,1*}} \frac{d\Omega_X}{dn_X} \quad \text{for } T < 0\ ^\circ C \quad (2)$$

In equation (1), $n_{IN\_BIO,X}$ is the number mixing ratio of INP active at temperature T for given species X; Ω_X is the total surface area mixing ratio of particles with diameters D_X greater than 0.1 µm; $d\Omega_X/dn_X \approx \pi D_X^2$. The normalized size distribution of given bioaerosol species is given by $dn_X/d\log D_X$. In Eq (2), H_X is the empirically determined fraction that inhibits nucleation in substantially water-subsaturated conditions. The factor ξ varies between 0 to 1 and considers the fact during laboratory experiments drop freezing was not observed at temperatures warmer than a certain threshold in the laboratory observations. The parameter $\omega_{X,1*}$ depends on bioaerosol type with the dimensions of area (m²). The values of $\omega_{X,1*}$ shown for PLN and DTS are 0.1 m². For FNG and BCT the values of $\omega_{X,1*}$ are 9.817×10^{-5} and 9.12×10^{-5} m² respectively. The slope of the fitted curve (γ_X) has a constant value of 0.5 C^{-1}.

The concentration of algal particles at the ATTO site was much smaller than our detection threshold, so we could not use a similar empirical treatment for ALG. The frozen fraction for the algal particles (Diatom cell, Thalassiosira pseudonana) available in the

literature is used to estimate INPs from ALG (Wilson et al. 2015). The frozen fraction is given by eq. (3)

$$f_{algae}(T) = A_1 + \frac{(A_2 - A_1)}{1 + 10^{(B+T) \times p}} \qquad (3)$$

where $A_1 = -0.03, A_2 = 0.993, B = 27.73,$ and $p = 0.399$.

Also $f_{algae}(T) = 0$ at $T > -24\,^oC$ and $f_{algae}(T) = 1$ at $T < -35\,^oC$

For the given concentration of algal particles in the air (n_{algae}) the active INP from ALG is given by

$$n_{IN\_BIO,X} = f_{algae} \times n_{algae} \quad (4)$$

4. Influence of PBAP on radar reflectivity, precipitation, and radiative flux:

Figure S8a shows the effects of PBAP on the simulated radar reflectivity for the whole storm. When compared to the control run, there is no significant difference in the simulated radar reflectivity of the perturbed simulations ($< 4\%$). Figure S8b depicts the sensitivity of the total surface precipitation rate averaged over the domain to the changes in total PBAPs. The peak in surface precipitation rate is boosted by about 10% in the very high-PBAP cases compared to the control run. In remaining perturbed simulations, changes in surface precipitation rate are less than 5% when compared with the control run. The contribution from the stratiform component of rain is higher in the total amount of rain (90%) as compared to the convective rain (remaining 10%) (see Fig.S8c and S8d). Convective rainfall is more sensitive to the changes in PBAPs than stratiform rainfall. The increase in PBAPs by 100-fold results in a 50% higher peak of convective rainfall rate as compared to the control run.

The changes in accumulated surface precipitation due to PBAPs are shown in Table S4. The spatial distribution of accumulated surface rainfall shows considerable variation associated with changes in PBAPs (Figure S9). However, the overall effect of PBAPs on accumulated surface precipitation is minimal ($< 4\%$).

Figure S10 shows the domain averaged vertical profiles of shortwave, longwave fluxes, and cloud fractions for the different sensitivity tests considered here. Among all the sensitivity runs, only the high-PBAP case showed a noticeable effect on shortwave flux, which was 2% higher than the control run. The variations in longwave fluxes were less than 1%. The vertical profiles of cloud fraction show that a 100-fold increase in total PBAPs results in a 10% higher cloud fraction between 8 and 12 km. However, the overall change in cloud fraction from a 100-fold increase in PBAP is less than 4% as shown in Table S4. The cloud fraction in other sensitivity runs was less sensitive to the changes in PBAP loadings. The ultra high-pbap case simulated a predicted 10% higher cloud fraction than the control run (see Table S4)
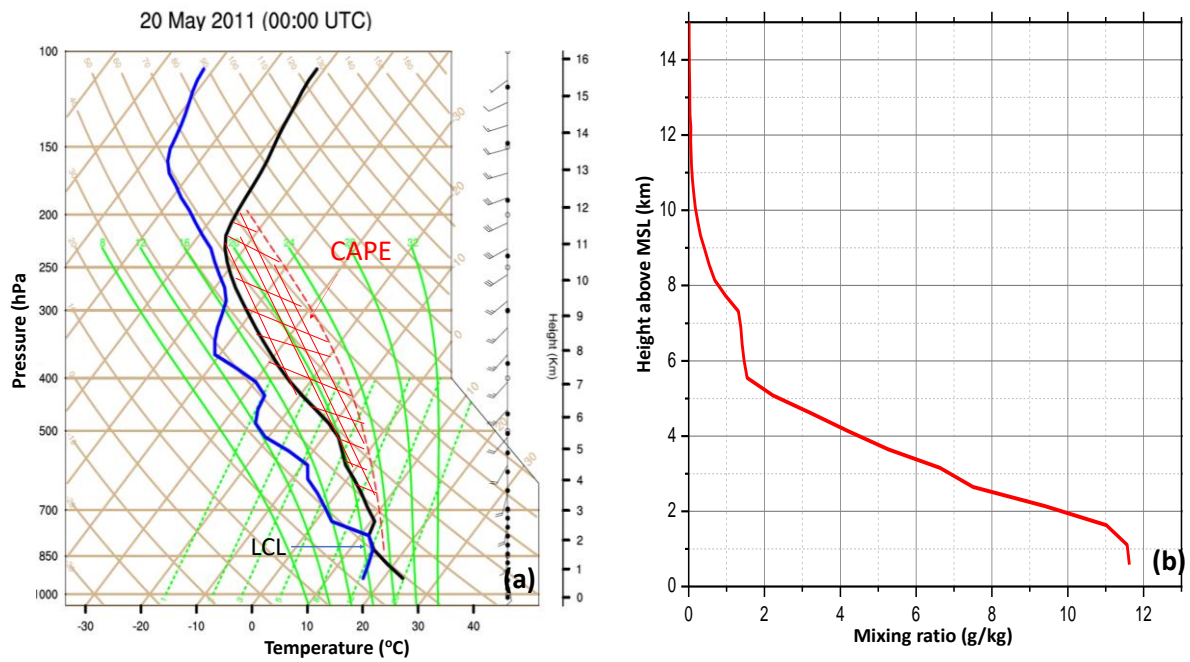
Figure S1. (a) The *skew T* plot from May 20, 2011, sounding. The air temperature is represented by the solid black line, while the dew point temperature is represented by a solid blue line. The moist adiabat is represented by a dotted red line. The shaded region between moist adiabat and temperature line represents convective available potential energy (CAPE). The LCL is also mentioned in the plot. (b) Vertical profile of water vapor mixing ratio on 20 May 2011 at 00 UTC.
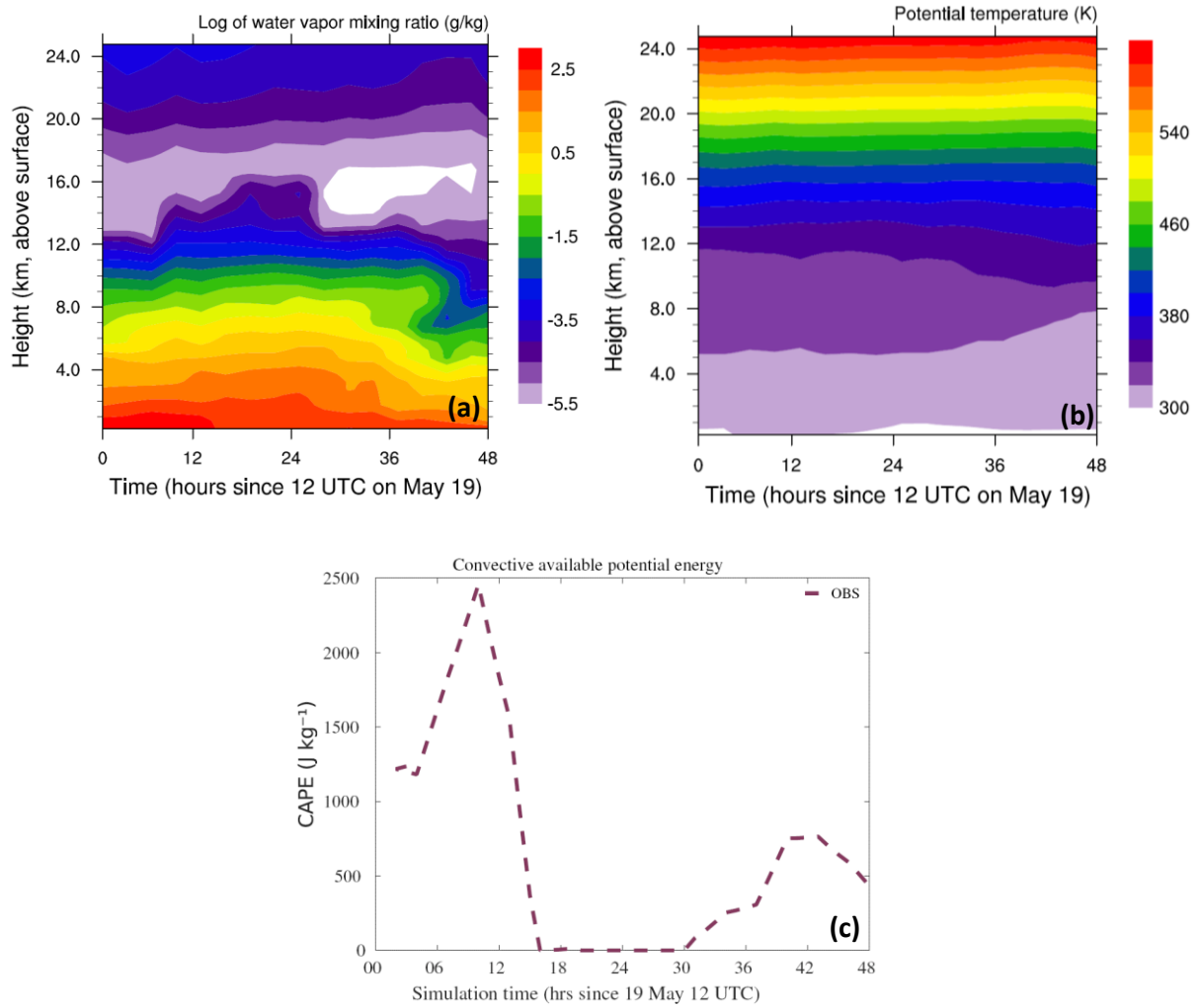
Figure S2: The time height plot of large-scale forcing used for the simulation including (a) water vapor mixing ratio and (b) potential temperature. (c) Variation in CAPE with time since 12 UTC on May 19 is also shown.
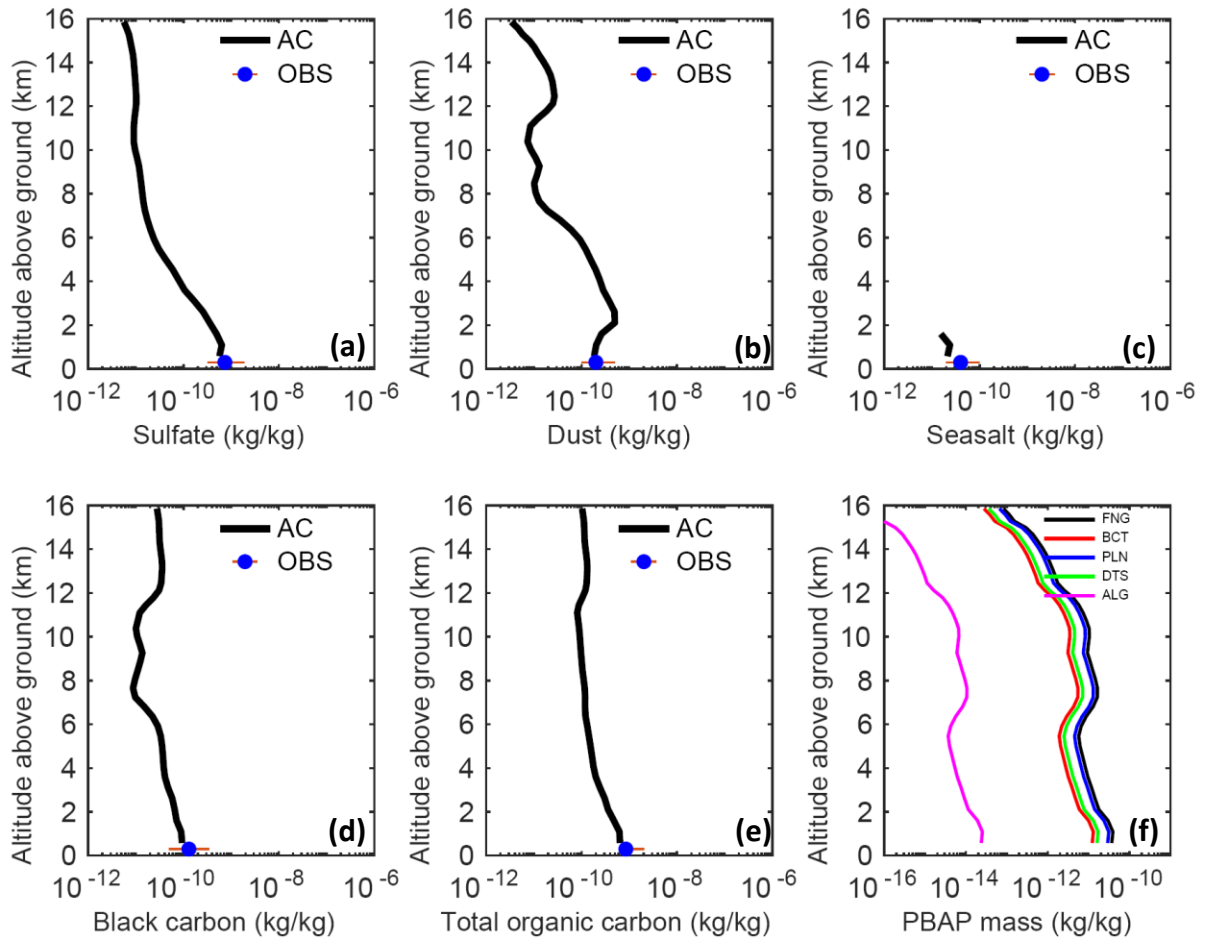
Figure S3: Vertical mass distribution of various aerosol species considered as in the AC model including (a) sulfate, (b) dust, (c) sea salt, (d) black carbon, and (d) total organic carbon. The observations from IMPROVE are also shown in each plot by the blue marker. (f) The vertical profiles of the mass of the various PBAP groups from the AC model are also shown
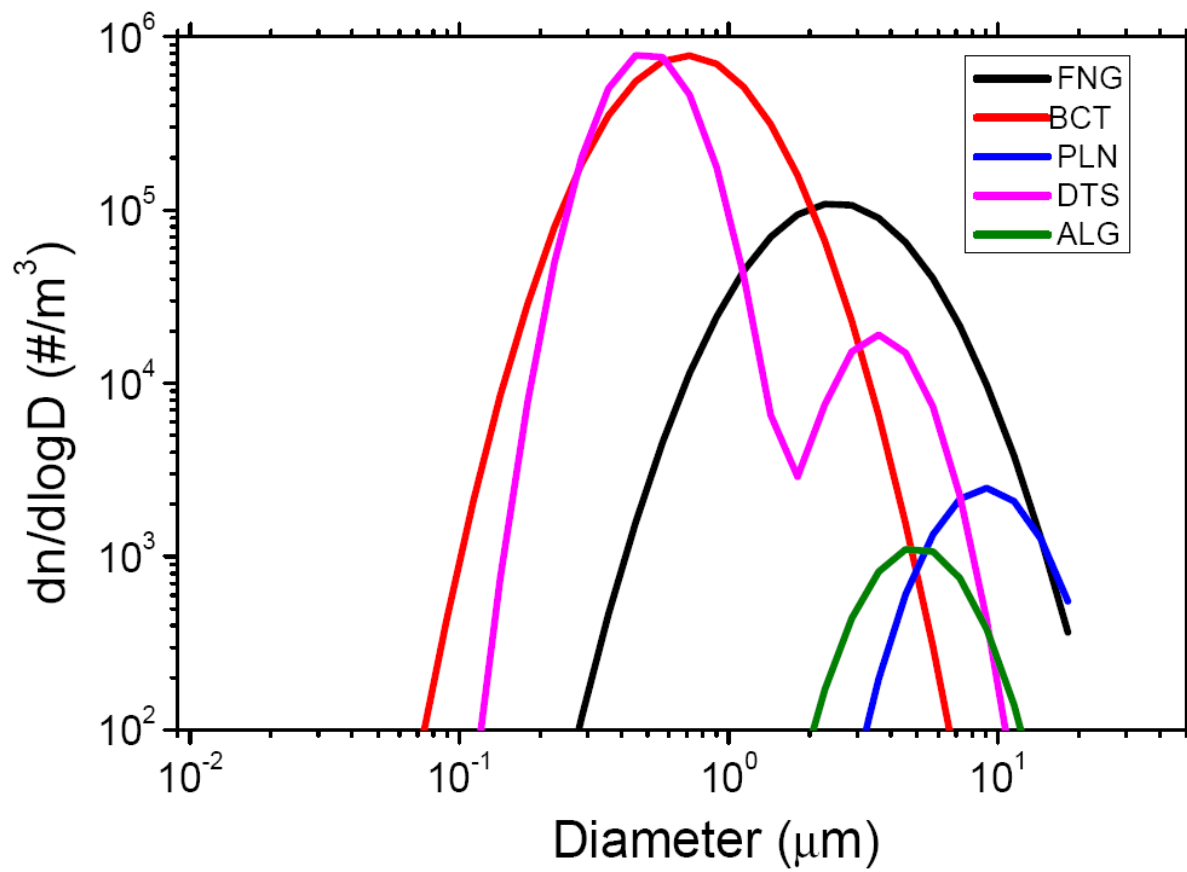
Figure S4: Size distribution of various PBAP groups prescribed in the AC model. The size distribution shown here is at the surface.
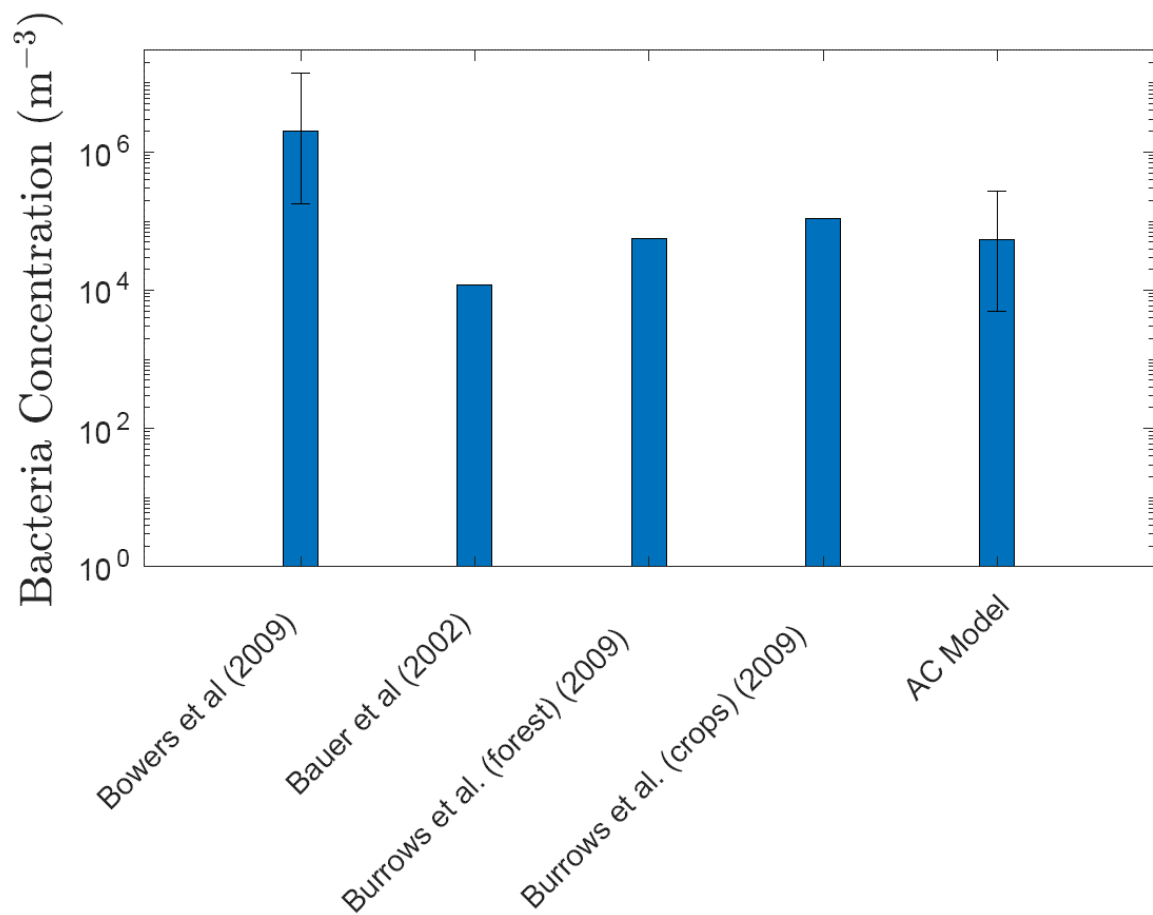
Figure S5: The comparison of model estimated bacterial number concentration with various observations.
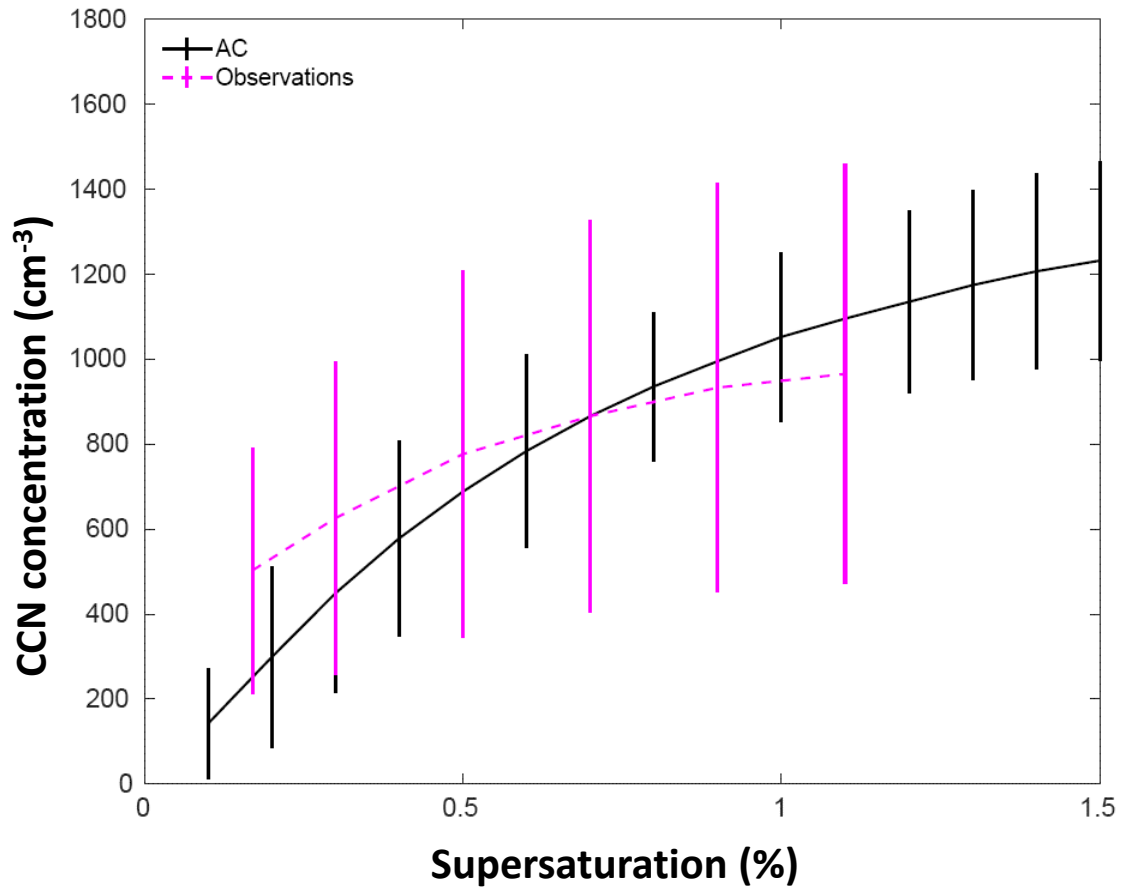
Figure S6. The CCN spectrum from AC for a simulated squall line case on May 20, 2011, for an environment 500 meters above MSL. The predicted CCN spectrum is compared to the observed CCN spectrum at the SGP CF (300 m above MSL). The error bars on the model predicted CCN concentration are associated with uncertainties in the input values of mass mixing ratios of various aerosol species that act as CCN.
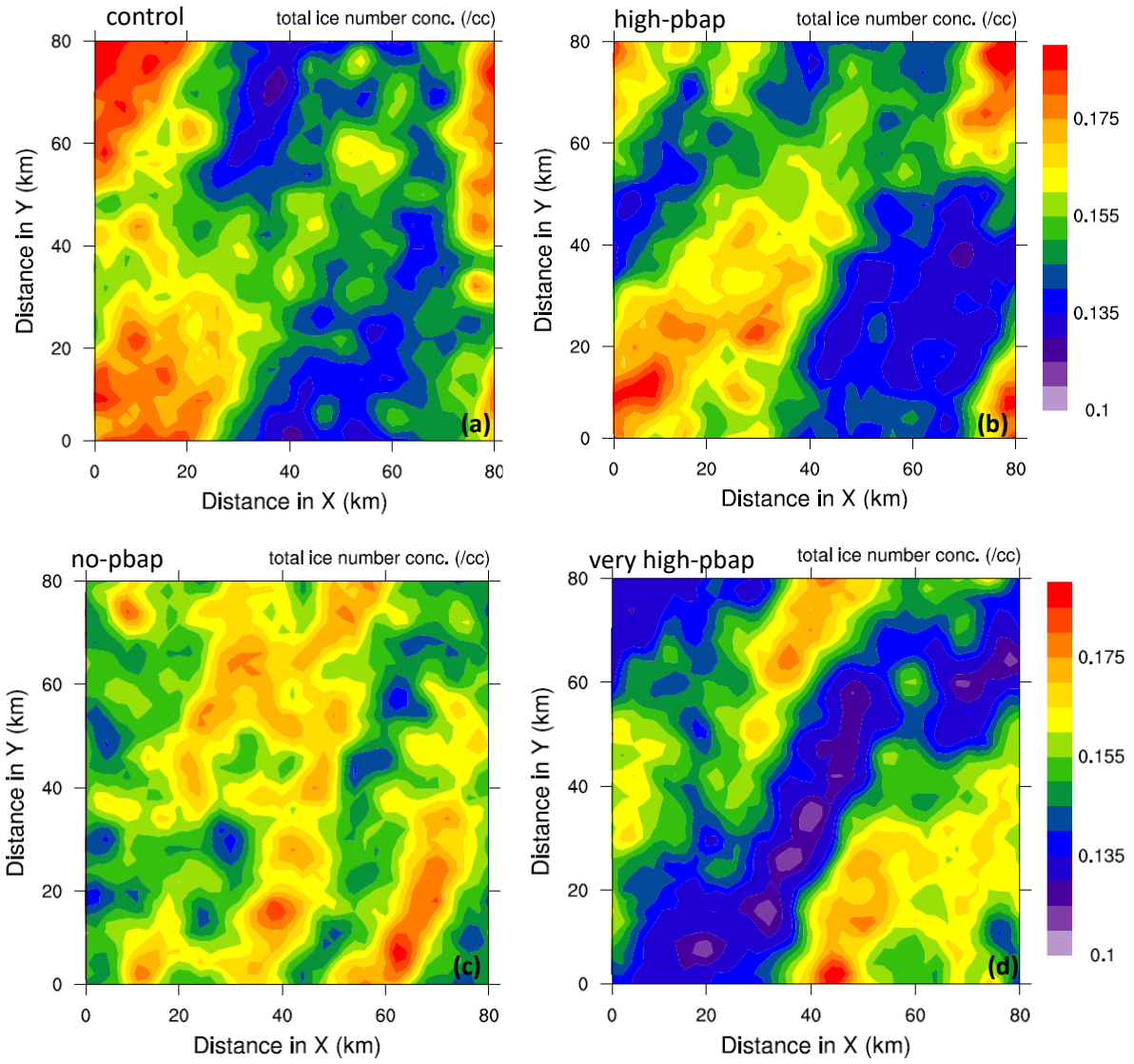
Figure S7: Spatial distribution of vertical averaged total ice number concentration for the whole storm for various sensitivity tests.
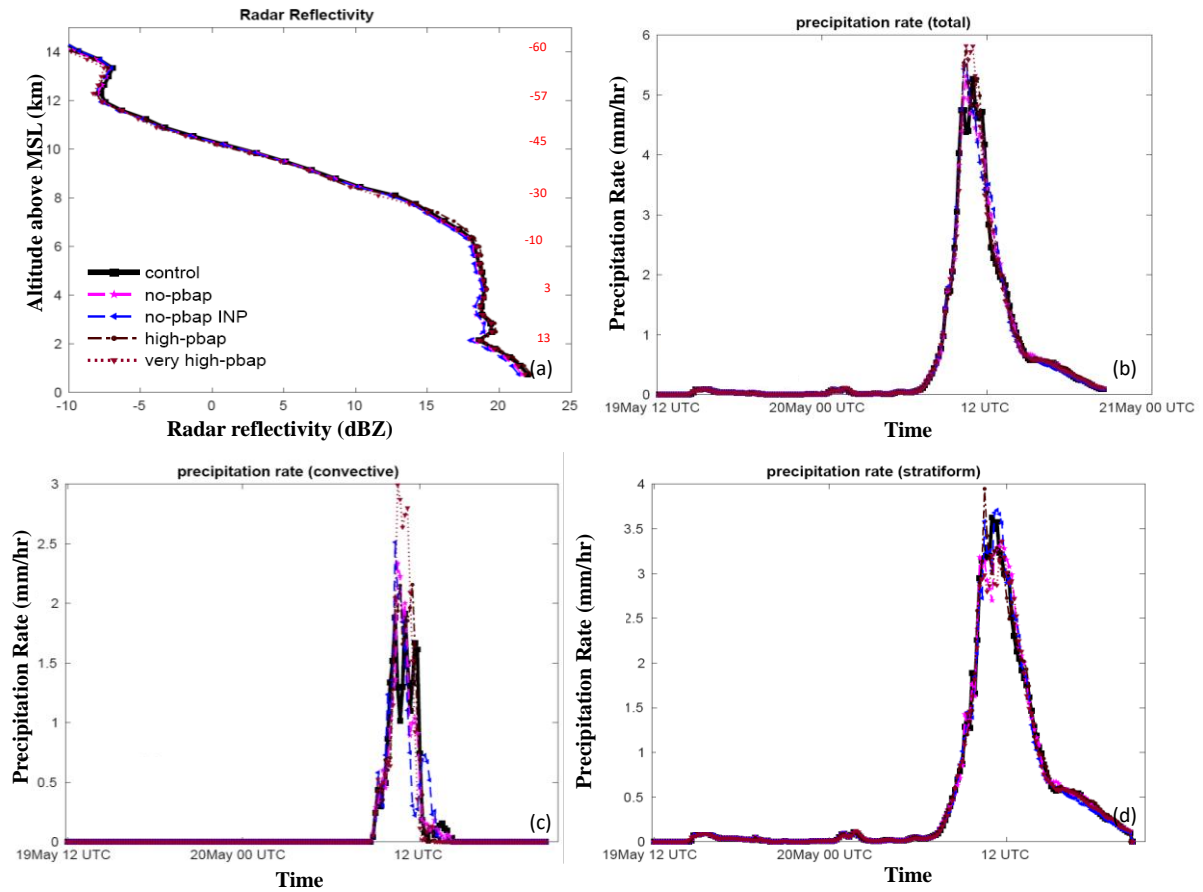
Figure S8: The vertical profiles of (a) radar reflectivity are shown for simulations involving changes in PBAP. (b)The temporal evolution of the total surface precipitation rate averaged over the domain is also shown. The time series of surface precipitation rate averaged over the domain is also shown separately for (c) convective and (d) stratiform regions. All the vertical profiles shown here are averaged for the whole domain.
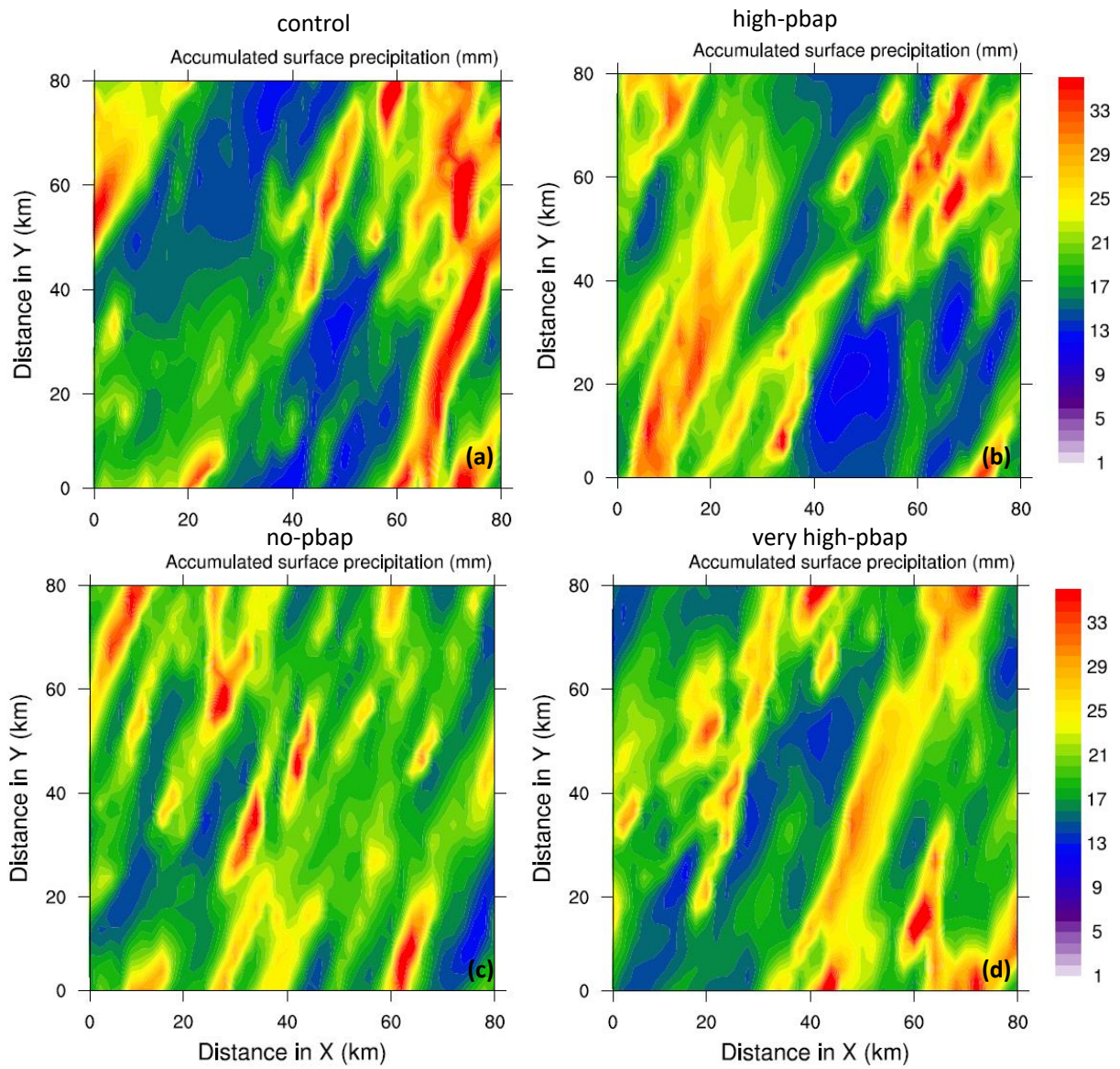
Figure S9: Spatial distribution of accumulated surface precipitation for the whole storm for various sensitivity tests.
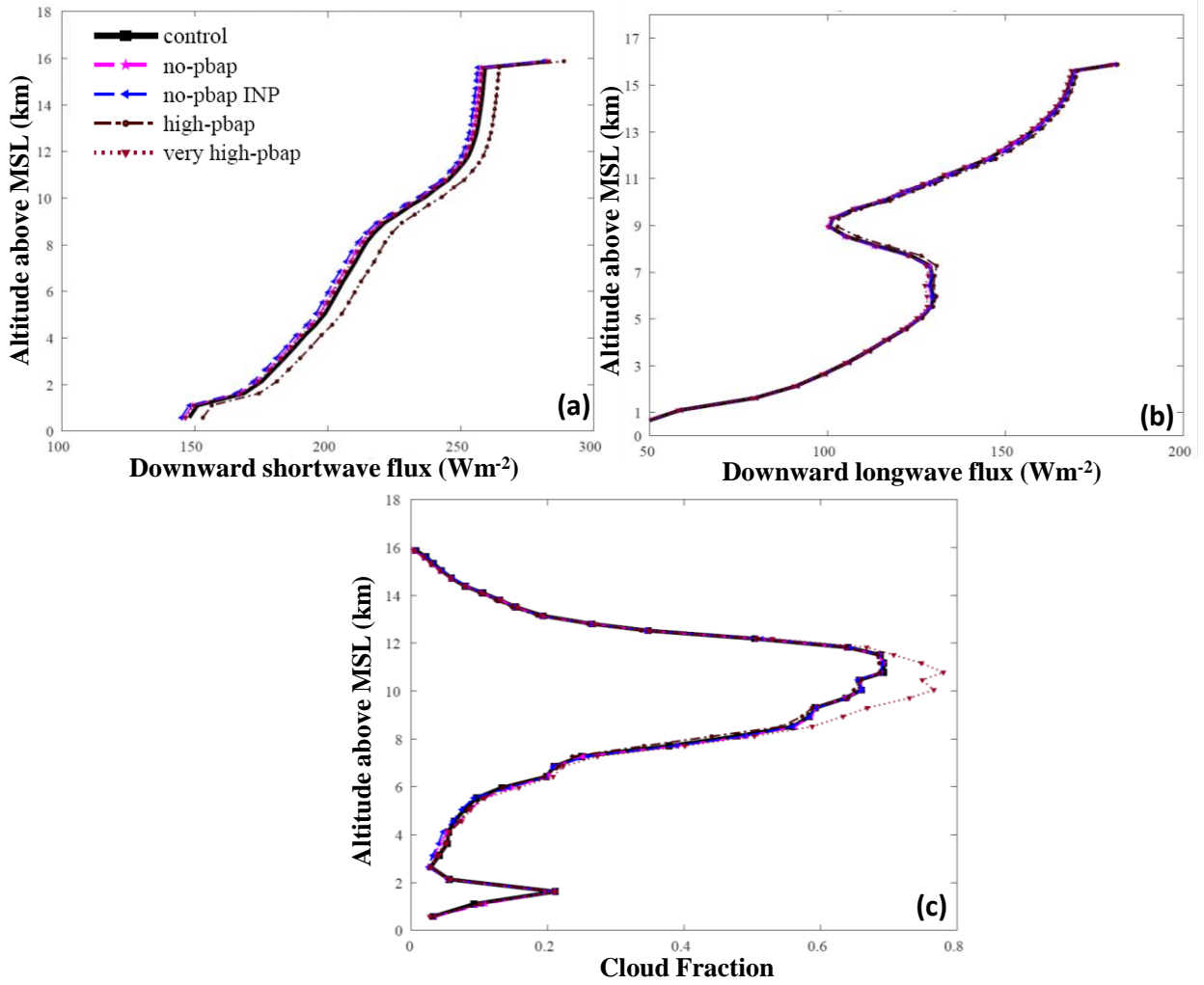
Figure S10: The domain averaged vertical profiles of downward components of (a) shortwave flux, (b) longwave flux, and (c) cloud fraction for various sensitivity experiments. The data shown here is an unconditional average over the whole duration and domain of each simulation. All the vertical profiles shown here are averaged for the whole domain.

Table S1: Details of aircraft instruments used in this study.

Instrument	Measurement	Typical range
Cloud imaging probe (CIP) by Droplet Measurement Technologies (DMT)	Size distribution of cloud and precipitation particles	0.025–1.5 mm (0.2-1 mm for model validation in the current study)
2D cloud imaging probe (2D-C) (PMS)	Size distribution of cloud and precipitation particles	0.03–1.0 mm (0.2-1 mm for model validation in the current study)
Cloud droplet probe (CDP) (DMT)	Cloud droplet spectra	2–50 μm
High-volume precipitation spectrometer, version 3 (HVPS-3) (SPECinc)	Precipitation particle spectra	0.15–19.2 mm
King hot-wire liquid water content (LWC) probe (DMT)	Cloud liquid water	0.01–5 g m^{-3}
Temperature probe	Ambient air temperature	–
Static pressure sensor	Ambient air pressure	–

Table S2: The mass mixing ratio of aerosol species based on IMPROVE observations which are used as input to AC.

Aerosol species	Mass mixing ratio ($\mu g/m^3$)
$(NH_4)_2SO_4$	0.56
Dust	0.18
Sea salt	0.021
Black carbon	0.093
Soluble organic carbon (80 % of TOC)	0.45
Insoluble organic carbon (20 % of TOC)	0.18
PBAPs (50% of Insoluble organic carbon)	FNG=0.036; BCT=0.012; PLN=0.028; DTS=0.016; ALG=0.000022

Table S3: Description of various sensitivity simulations carried out in the current study. The corresponding figures for each simulation are also mentioned.

Simulation	PBAP included	Changes in initial PBAP mass	Cloud processes switched on/off	Corresponding figures
control (five ensembles)	ALL PBAPs act as CCN and INP	-	All cloud processes in the AC are on	
no-PBAP (five ensembles)	No PBAP can act as CCN and INP	All PBAPs mass was set to zero	Same as control	Figures 6,7,8, S8, S10
no-PBAP INP (five ensembles)	No PBAP can act as INP (CCN activity of PBAP is on)	-	Same as control	Figures 6,7,8, S8, S10
high-PBAP (five ensembles)	Same as control	All PBAPs mass was boosted by a factor of 10	Same as control	Figures 6,7,8, S8, S10
very high-PBAP (five ensembles)	Same as control	All PBAP mass boosted by a factor of 100	Same as control	Figures 6,7,8, S8, S10
ultra high-PBAP (five ensembles)	Same as control	All PBAP mass boosted by a factor of 1000	Same as control	Figure 6, 7
no-sublimation breakup	Same as control	-	SIP from sublimation breakup is off	Figure 9
No-collisional ice-ice breakup	Same as control	-	SIP from the collision between ice particles is off	Figure 9
No-secondary	Same as control		All SIP	Figures 9, 10

			mechanisms are off	
very high-PBAP with no secondary	Same as control	All PBAP mass boosted by a factor of 100	All SIP mechanisms are off	Figure 10

Table S4: Changes in mean cloud macro and microphysical properties associated with various sensitivity tests carried out.

Simulations	Ice number conc. (cm^{-3})			LWC (g/m^3)			Downward shortwave radiation flux (W/m^2)	Downward longwave radiation flux (W/m^2)	Cloud cover (%)	Accumulated surface precipitation (mm)
	Total	*Convective*	*Stratiform*	*Total*	*Convective*	*Stratiform*				
control	0.76	0.47	0.052	0.128	0.285	0.063	165.28	136.8	0.231	20.10
no-PBAP	0.72	0.46	0.057	0.13	0.281	0.069	163.42	139.6	0.224	19.92
no-PBAP INP	0.80	0.48	0.053	0.13	0.287	0.068	164.7	137.3	0.229	20.14
high-PBAP	0.71	0.44	0.050	0.14	0.30	0.068	168.1	138.6	0.227	19.96
very high-PBAP	0.73	0.44	0.043	0.135	0.29	0.068	166.07	138.8	0.24	20.04
ultra high-PBAP	0.60	0.48	0.03	0.141	0.29	0.070	159.4	133.1	0.26	20.70
no-sublimation breakup	0.84	0.52	0.054	0.12	0.26	0.065	184.1	144.9	0.21	20.52
No-collisional ice-ice breakup	1.82	1.35	0.21	0.15	0.32	0.082	153.4	123.6	0.24	15.41
No-secondary	1.89	1.45	0.18	0.15	0.30	0.08	158.6	115.7	0.26	24.23
very high-PBAP with no secondary	1.85	1.38	0.20		0.30	0.085	208.3	127.8	0.28	23.95

Table S5: Changes in mean cloud macro and microphysical properties associated with various sensitivity tests carried out at T > -35°C.

Simulations	Ice number conc. (cm^{-3}) at T > -35°C		
	Total	Convective	Stratiform
control	0.10	0.087	0.019
no-PBAP	0.10	0.873	0.022
no-PBAPs INP	0.09	0.081	0.019
high-PBAP	0.11	0.092	0.018
very high-PBAP	0.10	0.084	0.017
ultra high-PBAP	0.098	0.082	0.015
no-sublimation breakup	0.108	0.089	0.020
No-collisional ice-ice breakup	0.13	0.111	0.069
No-secondary	0.011	0.105	0.081
very high-PBAPs with no secondary	0.010	0.097	0.065

References:

1. Field, P. R., Heymsfield, A. J., & Bansemer, A.: Shattering and Particle Interarrival Times Measured by Optical Array Probes in Ice Clouds, Journal of Atmospheric and Oceanic Technology, 23(10), 1357-1371, 2006.

2. Korolev, A. V., Emery, E. F., Strapp, J. W., Cober, S. G., Isaac, G. A., Wasey, M., & Marcotte, D.: Small Ice Particles in Tropospheric Clouds: Fact or Artifact? Airborne Icing Instrumentation Evaluation Experiment, Bulletin of the American Meteorological Society, 92(8), 967-973, 2011.